



Original Paper

Numerical study on erosion behavior of sliding sleeve ball seat for hydraulic fracturing based on experimental data



Xuan-Li Zhou ^a, Yan-Bao Guo ^{a, *}, Qiu-Ju Xie ^a, De-Guo Wang ^a, Hyun C. Yoon ^{b, c}

^a College of Mechanical and Transportation Engineering, China University of Petroleum, Beijing, 102249, China

^b Harold Vance Department of Petroleum Engineering, Texas A&M University, College Station, TX, 77843, United States

^c Korea Institute of Geoscience and Mineral Resources, Daejeon, 34132, South Korea

ARTICLE INFO

Article history:

Received 24 February 2022

Received in revised form

31 August 2022

Accepted 31 August 2022

Available online 6 September 2022

Edited by Xiu-Qiu Peng

Keywords:

Multistage fracturing

Sliding sleeve ball seat

Erosion wear

Erosion model

Fluent simulation

ABSTRACT

The sleeve sealing ball seat is one of the important components in the multistage fracturing process of horizontal wells. The erosion and wear of the surface will decrease the sealing performance of the fracturing ball and the ball seat. This leads to pressure leakage during the fracturing process and fracturing failure. In this paper, combined with the actual ball seat materials and working conditions during the fracturing process, the erosion tests of ductile iron and tungsten carbide materials under different erosion speeds, angles, and mortar concentrations are carried out. Then the erosion test results were analyzed by mathematical fitting, and a set of erosion models suitable for sliding sleeve setting ball seat materials were innovatively established. For the first time, this paper combines the erosion model obtained from the experiment and the computational fluid dynamics (CFD) with Fluent software to simulate the erosion of the ball seat. Based on the simulation results, the morphology of the sliding sleeve seat ball after erosion is predicted. Through analysis of the test and simulation results, it is showed that the erosion rate of tungsten carbide material is lower and the wear resistance is better under the condition of small angle erosion. This research can offer a strong basis for fracturing site selection, surface treatment methods, and prediction of failure time of ball seats.

© 2022 The Authors. Publishing services by Elsevier B.V. on behalf of KeAi Communications Co. Ltd. This is an open access article under the CC BY-NC-ND license (<http://creativecommons.org/licenses/by-nc-nd/4.0/>).

1. Introduction

Horizontal well with multistage fracturing technology is crucial to increase the productivity of oil development in shale gas fields, and mechanically-packed staged fracturing is a key component (Nandlal and Weijermars, 2019). This method utilizes low-density balls and sliding sleeve ball seats to set and hold the pressure required for fracturing processes through horizontal wells (Pei et al., 2014; Zheng et al., 2017). The schematic principle is shown in Fig. 1. For hydraulic fracturing, the general fracturing fluid is a sand (or proppant)-carrying fluid. As fracturing displacement and sand ratio increases, the effect of fracturing proppants on the erosion and abrasion of components for a long time becomes increasingly obvious. There will be a loss of material inflow parts which will fail in the maximum service life of the equipment to meet fracturing requirements at the construction site, failing the

whole fracturing process (Zhang et al., 2017). Foreign fracturing technology has developed to a relatively advanced level. The RapidFrac completion system launched by Halliburton is mainly composed of DeltaStim sliding sleeves and Swellpacker packers (Miao and Zhao, 2017). Each section is composed of a DeltaStim sliding sleeve and a fast-fracturing sliding sleeve to achieve multi-point fracturing. At the same time, the continuous pumping fracturing process is adopted, so the cycle time can be shortened and the consumption of clean water can be reduced. Halliburton has developed a new type of electronic sliding sleeve that can achieve an unlimited number of fracturing zones and improve the efficiency of sliding sleeve operations. This design increases the reliability, flexibility, and durability of multi-stage hydraulic fracturing, and is suitable for use in extended reach wells and an infinite number of formations. As part of Weatherford's ZoneSelect™ completion system, the ball-throwing fracturing sleeve can help operators complete up to 59 stages of multi-stage fracturing operations at a time, thereby improving operational efficiency and saving operation time (Miao and Zhao, 2017). I-ball™ fracturing sleeve of Weatherford can open all the sliding sleeves in the

* Corresponding author.

E-mail address: gyb@cup.edu.cn (Y.-B. Guo).

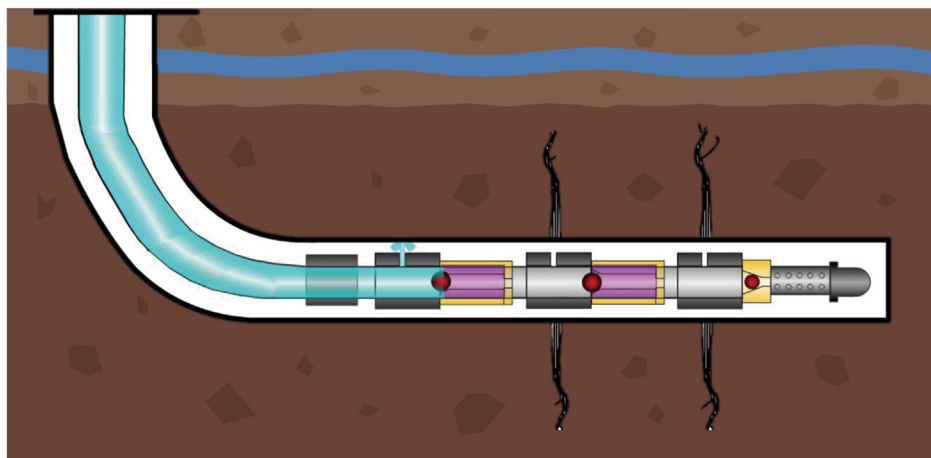


Fig. 1. Multi-stage fracturing diagram.

horizontal section by using the same diameter ball and ball seat. I-ball™ fracturing sleeve helps to optimize the placement of proppants and increase the permeability, porosity, and recovery of the reservoir. However, these companies are still in their infancy in research on the erosion and wear laws and life predictions of the ball seats of different grades and materials under long-term erosion. The influence of different working conditions (erosion speed, erosion angle, particle radius, etc.) on the erosion rate of the ball seat material is still unclear.

To increase the efficiency of horizontally staged fracturing and decrease maintenance and overhaul times of equipment, scientists have conducted long-term research on the mechanism of the destruction of components caused by the impact of sand-containing water and figured out some in various perspectives. Zheng et al., used 3D computational fluid dynamics (CFD) to analyze the flow characteristics in the ball seat structure, including the impact velocity, pressure, and sand concentration. The effect of the cone angle and other parameters in the ball seat structure on the flow properties and erosion was mainly studied, and the structure of the sliding sleeve ball seat has been optimized (Zheng et al., 2016). Based on computational fluid dynamics, Zhu et al., simulated the erosion distribution of a U-bend composed of two 90° elbows. Erosion mainly occurs on the dome, the lower surface of the U-shaped pipe, and the downstream pipe (Zhu and Qi, 2019). Zhang et al., developed erosion and wear test equipment to study the erosion of high-pressure pipelines during mudflow. Based on the experimental data, the erosion and wear distribution of the pipeline are simulated in the Fluent software (Zhang et al., 2016). Zheng et al., used finite element analysis (FEA) and experimental methods to study the strain distribution of aluminum alloy fracturing balls under different fracturing pressures. The largest deformation occurs in the contact area between the fracturing ball and the ball seat (Zhang et al., 2016a). Besides, many scholars have explored the influence of different parameters of erosion and wear of materials. Jung et al., applied experiments to study the influence of impact velocity, impact angle, and particle number on the erosion behavior of 9Cr–1MoVNb material at high temperatures (Jung and Kim, 2020).

However, most of the erosion wear models are based on theoretical analysis, and only a few of them are obtained under real field conditions. Although Fluent has its erosion wear model, still the relationship between speed, angle, particle size, and wear rate remain obscure. Currently, there are a lot of empirical and semi-empirical formulas such as for elbows, reducers, and so on, which are summarized under specific experimental environments and

materials. But it is not suitable for all wear situations. Due to the complex fracturing conditions of horizontal wells and the large number of stages, it is difficult to directly conduct experiments on sliding sleeve ball seats at all levels. Therefore, it is necessary to use finite element analysis software to establish erosion models of different materials to predict the surface morphology of the ball seat after long-term erosion, so as to calculate the failure time of the ball seat. At the same time, due to the different erosion properties of different ball seat materials, the morphology of the ball seat surface after erosion is different. Therefore, the establishment of erosion models for commonly used ball seat materials is helpful for the selection of surface treatment methods for different stages of ball seats. In addition, the severity of erosion wear of the sliding sleeve ball seat is not only related to the properties of the base material, but also closely related to the flow state inside the runner. Reasonable diversion and changing the movement trajectory of the sand particles can effectively avoid the collision of the sand particles on the ball seat seal, and solve the serious erosion and wear problem of the fracturing ball seat. Therefore, the establishment of the erosion model of the finite element analysis of the sliding ball seat can provide theoretical guidance for the optimization of the geometric structure of the sliding ball seat and the design of the surrounding flow structure from the perspective of the internal flow field of the sliding ball seat. Therefore, this study summarizes models for analyzing the erosion and wear of different materials based on experiments, and analyzes the erosion and wear experimental laws for sliding sleeve ball seat materials. This can be utilized in providing a more reliable reference for the optimal design of the ball seat and in the prediction of the service life of the ball seat during the production process.

2. Experimental investigations

2.1. Experimental conditions

An erosion test machine (Fig. 2) was used to perform erosion tests on ductile iron and WC materials. The samples are thoroughly cleaned and then installed in the erosion equipment for testing. The parameters studied in this experiment include erosion rate, erosion angle, and concentration of erosion particles. Erosion test conditions and materials are shown in Table 1.

Before the experiment, a mortar with a concentration of 15% was mixed in the tank. Table 2 shows the sand concentration measured from the nozzle outlet before, during and after the test. The calculation shows that the average nozzle sand concentration is 15.017%.

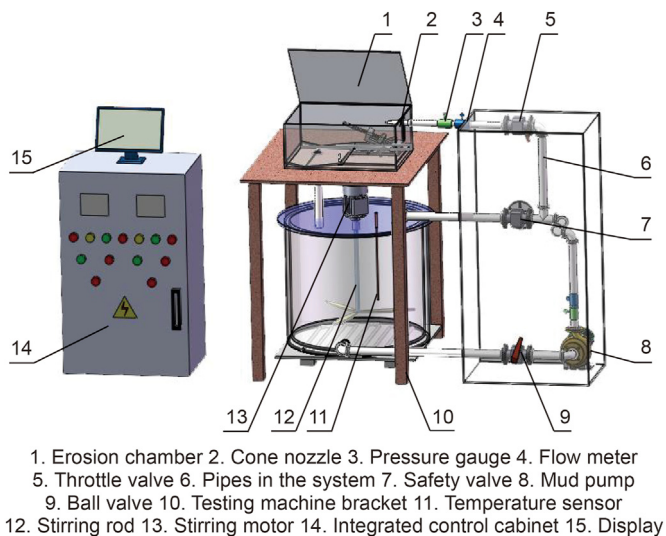


Fig. 2. Schematic diagram of erosion test machine.

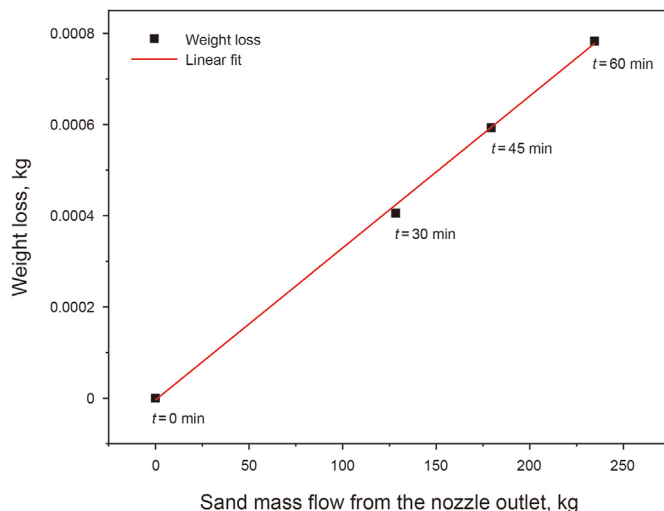


Fig. 3. Relationship between the weight loss of the sample and sand mass flow from the nozzle outlet.

Table 1
Erosion test conditions and materials.

Test parameter	Parameter values
Materials	Ductile iron, WC coated ductile iron
Style of particles	Ceramsite
Size of particles, μm	up to 400
Nozzle diameter, mm	8
nozzle to the specimen spacing, mm	20
Concentration of erosion particles	5%–30% (mass concentration)
Erosion Angle, °	15, 30, 45, 60, 90
Erosion speed, m/s	12.5, 17.5, 22.5, 27.5, 30
Temperature, °C	20
Erosion time, h	0.5

Changes in sand conditions can be judged by testing the relationship between the weight loss of the sample and sand mass flow from the nozzle outlet after erosion for different time (Wang et al., 2019). Under the condition of erosion speed of 20 m/s, the weight loss of the sample was tested at 30 min, 45 min and 60 min after the start of the experiment, respectively. Fig. 3 shows the fitting curve of the weight loss of the sample and the sand mass flow from the nozzle outlet at different times. It can be seen from the figure that the weight loss of the sample increases linearly with the erosion time and the sand mass flow from the nozzle outlet. The linear trend indicated that the sand conditions did not change significantly during the erosion experiment (Nguyen et al., 2014). If the particle size and geometry of the sand changes, the erosion rate will change (Liu et al., 2014). Therefore, the PSD of sand did not change significantly over time in our experiments.

2.2. Evaluation method of erosion rate

The weight-loss method allows us to calculate the wear state of

the sample after the erosion test, and the formula can be written:

$$\epsilon = \frac{m_0 - m_1}{m_{sand}} \tag{1}$$

where ϵ is the erosion rate of the material, in mg/kg, and m_0 is the mass of the sample before erosion. m_1 is the mass of the sample after erosion, and m_{sand} is the quality of the sand grains that impacts the sample during the erosion process.

Equation (1) can also be divided by the material density ρ and converted into volume erosion rate ϵ_v with the formula:

$$\epsilon_v = \frac{m_0 - m_1}{\rho m_{sand}} \tag{2}$$

2.3. Experimental results

2.3.1. The relationship between erosion rate and angle

The experiments tested the erosion rate of two ball seat materials of ductile iron and WC when the erosion angle was 15°, 30°, 45°, 60° and 90°, and the calculated erosion velocity was 30 m/s. The particle diameter is 400 μm, and the particle concentration is 15%. The test results are used to get the erosion rate of the two ball seat materials as a function of the erosion angle, and the erosion curves are fitted with polynomials. The fitting curves and formulas are shown in Fig. 4, Table 3.

It can be seen intuitively from Fig. 4(a) that when the angle increases, the erosion of ductile iron first increases and then decreases, reaching a peak at around 30°. The rate of erosion rate increase between 15° and 30° is similar to the rate of erosion rate decrease between 30° and 45°. When the erosion angle is greater than 45°, the rate of erosion rate reduction begins to slow down.

Table 2
Sand concentration tests by sampling from the nozzle outlets.

Sample number	Dry sand weight, g	Solution weight, g	Sand concentration, %
1	278.1785	1567	15.076
2	238.7865	1353	15.001
3	182.9655	1039	14.973
Average sand concentration			15.017

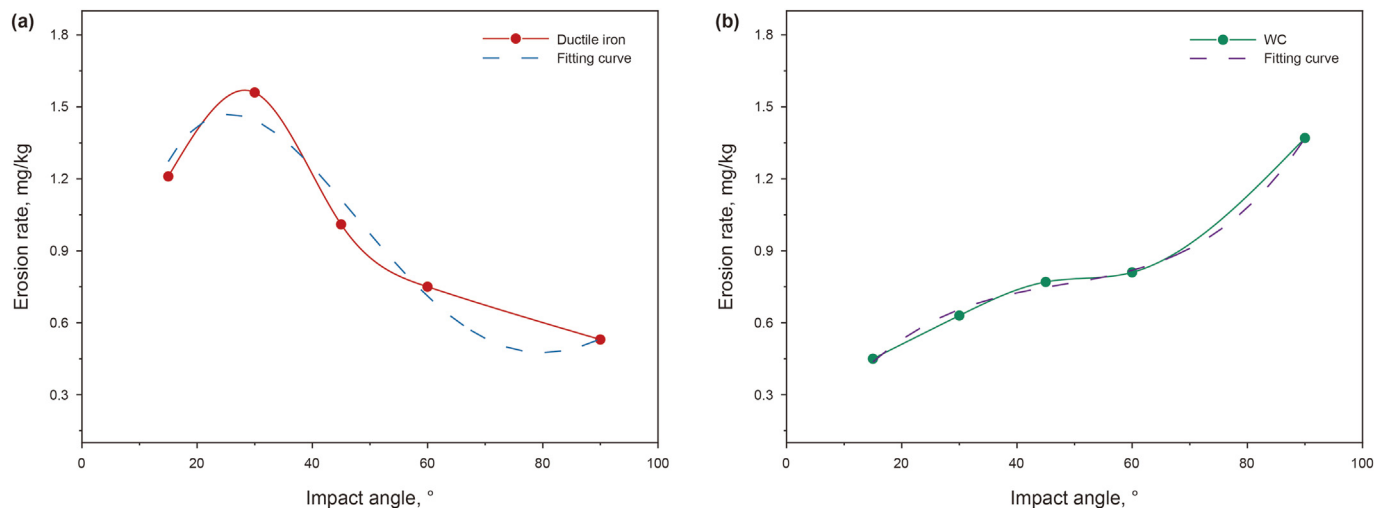


Fig. 4. Erosion fitting curves of ductile iron and WC materials at different angles.

Table 3

Fitting equations for the relationship between the impact angle and the erosion rate for the ductile iron and the WC materials.

Samples	Erosion fitting formula of the ball seat	Correlation coefficient
Ductile iron	$y = -1E - 7x^4 + 4E - 5x^3 - 0.0041x^2 + 0.1377x$	$R^2 = 0.9535$
WC	$y = 5E - 6x^3 - 0.0007x^2 + 0.0394x$	$R^2 = 0.997$

Therefore, the erosion damage of ductile iron near the erosion angle of 30° is the most serious. As the erosion angle increases, the erosion rate and wear degree of the material decrease continuously. Fig. 4(b) shows the variation curve of erosion rate of WC material with erosion angle. It can be seen that the erosion rate of WC increases with the increase of the erosion angle, and reaches a peak when the erosion angle is 90°. When the erosion angle is less than 60°, the erosion rate increases slowly; when the erosion angle is greater than 60°, the erosion rate increases rapidly with the increase of the angle.

2.3.2. The relationship between erosion rate and velocity

The erosion rates of the two ball seat materials when the impact velocities are between 12.5 m/s to 30 m/s have been studied. The particle diameter is 400 μm, and the particle concentration is 15%. The erosion angles in the test were 30° and 90°. The curves of erosion rates versus erosion velocities were fitted (Table 4 and Fig. 5). The results show that the correlation coefficients are all close to 1, so the fitting curve conforms to the actual erosion law of the material, and the erosion rate of the two materials has a power function relationship with the impact velocity.

2.3.3. Influence of sand concentration on erosion rate

In the early stage of the fracturing operation, the mortar concentration varies from 10% to 38%. In order to explore the influence of sand concentration on the erosion rate of sliding sleeve ball seats,

five mortar concentrations of 5%, 10%, 15%, 20%, and 30% were selected in this experiment to test ductile iron and WC materials. The test conditions are that the impact angle is 30° and the impact velocity is 30 m/s. The particle diameter is 400 μm.

It can be seen from Fig. 6 that the erosion rates of ductile iron and WC have the same trend of changing with the mortar concentration. When the mortar concentration is less than 15%, the erosion rate increases with the increase of the mortar concentration and reaches a peak value near 15%. But when the concentration continued to increase, the erosion rate did not change.

3. Establishment and verification of erosion model

It can be seen from the above experiments that when the size and shape of the sand particles are constant, the relationship between the erosion rate of the ball seat and the erosion angle and velocity can be obtained through the experiment. By analyzing the influence of impact angle and velocity on the erosion rate of sliding sleeve ball seats, the prediction model of erosion rate of the sliding sleeve in fracturing operation can be obtained. The model can effectively predict the erosion rate of the ball seat during the actual fracturing and provide a reference for controlling the real field fracturing parameters and the service life of the ball seat.

Table 4

Fitting equations for the relationship between erosion rate and erosion velocity of two materials at 30° and 90° erosion angle.

Impact angle	Samples	Erosion fitting formula of the ball seat	Correlation coefficient
30°	Ductile iron	$y = 0.0004x^{2.3922}$	$R^2 = 0.9986$
	WC	$y = 3E - 5x^{2.8666}$	$R^2 = 0.9925$
90°	Ductile iron	$y = 0.0003x^{2.2101}$	$R^2 = 0.9900$
	WC	$y = 5E - 5x^{2.9694}$	$R^2 = 0.9981$

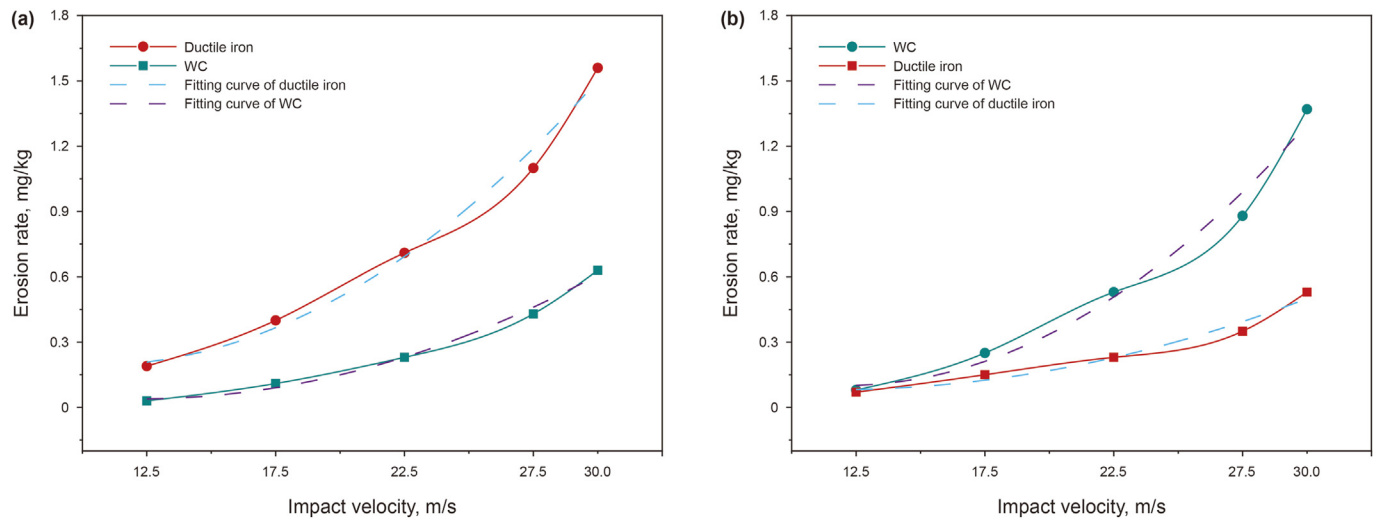


Fig. 5. Relationship between erosion rate and impact velocity of two materials at (a) 30° erosion angle (b) 90° erosion angle.

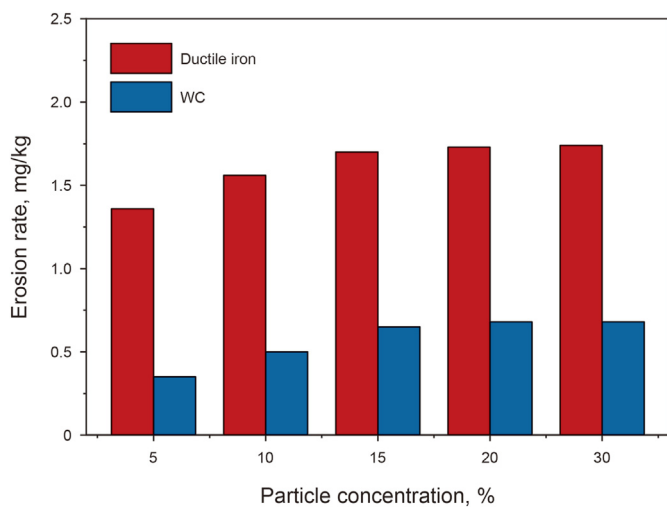


Fig. 6. Relationship between erosion rate and particle concentration of two materials.

3.1. Establishment of erosion model

The erosion rate characterization method in this paper is consistent with the Oka model of Hiroshima University, and it is the mass or volume loss caused by the impact of a unit mass of sand on the surface of the material. Therefore, it can be improved based on (Zhang et al., 2006), Oka model erosion rate is (Oka et al., 2005 (1), Oka et al., 2005 (2)):

$$\epsilon(\theta) = f(\theta)\epsilon(90) \tag{3}$$

$$f(\theta) = (\sin \theta)^{n_1} [1 + H_V(1 - \sin \theta)]^{n_2} \tag{4}$$

where $\epsilon(\theta)$ and $\epsilon(90)$ are the erosion rate at θ and 90° , respectively, in mg/kg; n_1 and n_2 are the coefficients related to the Vickers hardness (H_V) of the material. $f(\theta)$ is the erosion angle function, where when $\theta = 0^\circ$, $f(\theta) = 0$; when $\theta = 90^\circ$, $f(\theta) = 1$. However, the limitation of the Oka model is severe. The erosion angle function in the Oka model only considers the effect of material hardness. From the actual fracturing conditions, the erosion angle function is not only related to the hardness of the material, but also related to the

sand grain and other parameters such as its characteristics and fluid rheological conditions. Therefore, the Oka model is not suitable for simulating the erosion and wear of the ball seat in the actual fracturing operation. It is necessary to establish the erosion angle function through experiments. Both the American Erosion Corrosion Research Center and Det Norske Veritas obtained the erosion angle function through the polynomial fitting of the test data (Safari et al., 2017). Therefore, this study also utilizes the same method to obtain the erosion angle function. Under the same size of erosion particles, when the mortar concentration is greater than 15%, the erosion rate remains unchanged. On the basis of satisfying the actual fracturing conditions, the factors affecting the erosion rate of the ball seat material are the erosion angle and its velocity. Through the polynomial regression of the test data and the non-dimensionalization of the obtained polynomial based on the 90° test data, the erosion angle function of ductile iron and WC material can be obtained, as shown in formula (5):

$$f(\theta) = \sum_{i=1}^4 (-1)^{i+1} A_i \theta^i \tag{5}$$

In the formula, θ is the erosion angle. A_i is the coefficients obtained by transforming the polynomial dimensionless based on 90° . The values are shown in Table 5.

In the Oka model, $\epsilon(90)$ can be expressed as:

$$\epsilon(90) = KV^{b(v)} \tag{6}$$

where V is the erosion velocity, K is the fitting coefficient when the erosion angle is 90° , and $b(v)$ is the velocity index when the erosion angle is 90° . The values of K and $b(v)$ are shown in Table 4 (Erosion fitting formula of ball seat). Therefore, based on formulas (3)–(5), a prediction model of ball seat erosion rate suitable for fracturing conditions can be established:

$$\epsilon = KV^{b(v)} \sum_{i=1}^4 (-1)^{i+1} A_i \theta^i \tag{7}$$

where ϵ is the erosion rate of the ball seat materials, in mg/kg; K and $b(v)$ are the fitting coefficients and velocity index of the erosion rate at erosion angles of 90° , respectively. V is the erosion velocity. θ is the erosion angle, if $\theta = 90^\circ$, then $f(\theta) = 1$. Therefore, under actual

Table 5
Fit coefficient of erosion angle function of ductile iron and WC.

Model	A ₁	A ₂	A ₃	A ₄
Fitting parameters of ductile iron based on 90°	0.2598	0.0077	7.5 × 10 ⁻⁵	2 × 10 ⁻⁷
Fitting parameters of WC based on 90°	0.0288	0.0005	3.6 × 10 ⁻⁶	0

fracturing conditions, the calculation formula for the erosion rate of ductile iron and WC materials commonly used in oil fields is:

$$\epsilon_{DI} = 0.0003V^{2.2101} \left(-2E - 7\theta^4 + 7.5E - 5\theta^3 - 0.0077\theta^2 + 0.2598\theta \right) \quad (8)$$

$$\epsilon_{WC} = 5E - 5V^{2.9694} \left(3.6E - 6\theta^3 - 0.0005\theta^2 + 0.0288\theta \right) \quad (9)$$

In order to accurately simulate the ball seat in the Fluent software to obtain accurate service life and erosion wear conditions, the established erosion rate prediction model is compared with the erosion rate model in Fluent. Then, they are combined into the form of Eq. (10).

The formula for the erosion rate of particles to materials in ANSYS Fluent is:

$$R_{\text{erosion}} = \sum_{p=1}^{N_p} \frac{m_p C(d_p) f(\alpha) v^{b(v)}}{A_{\text{face}}} \quad (10)$$

where R_{erosion} is the erosion rate, kg/(m²·s); m_p is the particle mass; α is the erosion angle; $f(\alpha)$ is the particle erosion angle function; $b(v)$ is the velocity index; A_{face} is the erosion surface area of the material; $C(d_p)$ is a function of particle diameter. Among them, the specific values of these parameters $f(\alpha)$, $b(v)$, and $C(d_p)$ can be obtained by experiments.

It is determined through experiments that the speed exponents $b(v)$ of ductile iron and WC are 2.2101 and 2.9694, respectively. $f(\alpha)$ is shown in formula (5). When the erosion material is ductile iron, the value of $C(d_p)$ is 2×10^{-9} . When the eroded material is WC, the value of $C(d_p)$ is 1.6×10^{-10} . Finally, by referring to formulas (7)–(10), the erosion rate formula of ductile iron and WC material can be obtained:

$$R_{DI} = \sum_{p=1}^{N_p} \frac{m_p 2 \times 10^{-9} \left(-2 \times 10^{-7}\theta^4 + 7.5 \times 10^{-5}\theta^3 - 0.0077\theta^2 + 0.2598\theta \right) V^{2.2101}}{A_{\text{face}}} \quad (11)$$

$$R_{WC} = \sum_{p=1}^{N_p} \frac{m_p 1.6 \times 10^{-10} \left(3.6 \times 10^{-6}\theta^3 - 0.0005\theta^2 + 0.0288\theta \right) V^{2.9694}}{A_{\text{face}}} \quad (12)$$

In the formula, R_{SG} and R_{WC} are the erosion rates of ductile iron and WC respectively, in kg/(m²s); m_p is the particle mass; α is the erosion angle; V is the erosion speed; A_{face} is the surface area of erosion.

3.2. Validation of erosion model

The prediction model of erosion rate of ductile iron is verified by

regression through experiments, as shown in Fig. 7. Fig. 7(a) is about the impact angle and Fig. 7(b) is about the impact velocity on the erosion rate, respectively. The test conditions of Fig. 7(a) are temperature of 20 °C, particle diameter of 400 μm, particle concentration of 15%, and erosion angle of 30°. The test conditions in Fig. 7(b) are normal temperature, particle diameter of 400 μm, particle concentration of 15%, and erosion rate of 30 m/s.

It can be found from Fig. 7(a) that the calculated value of the model and the experimental value are very close: the deviation is small at 15°~30° (about 4%); the error is larger at 30°~60° (about 9%); the calculated value and the test value are basically in agreement at higher angles (greater than 60°). Fig. 7(b) shows that the calculated value of the model and the test value are very close to each other (the error is within 5%) and both show a consistent growth relationship.

The calculated value of the established erosion rate prediction model is highly consistent with the erosion rate obtained through experiments, and the maximum error is only within 10%. It can effectively predict the erosion and wear rate and service life of the ball seat in the various actual working conditions and provide an effective basis for the site.

4. Simulation investigation

4.1. The establishment of the runner geometry model

Horizontal well-staged fracturing technology has been widely used in unconventional reservoirs in China. The core is to expand the seepage area and increase the output of a single well by fracturing the horizontal section cracks according to the physical properties of the reservoir and the characteristics of oil and gas. The field logging permeability of the reservoir is $1.19 \times 10^{-3} \mu\text{m}^2$, the viscosity of the formation crude oil is 5.32 mPa·s, and the average formation pressure coefficient is 1.22 MPa/100m. Reservoir sand-

stone is relatively dense and mudstone is less. The wellbore is smooth and stable, and the difference between the maximum and minimum principal stresses of the rock is very small. The ball-throwing sleeve split-layer fracturing technology can individually and accurately control each fracturing well section to realize the staged production of horizontal wells and shorten the fracturing operation time.

ANSYS Fluent is often used to simulate the motion characteristics of fluids (Sepehr et al., 2019). The horizontal well fracturing in an oil field typically has a total of 21 stages. The first stage uses

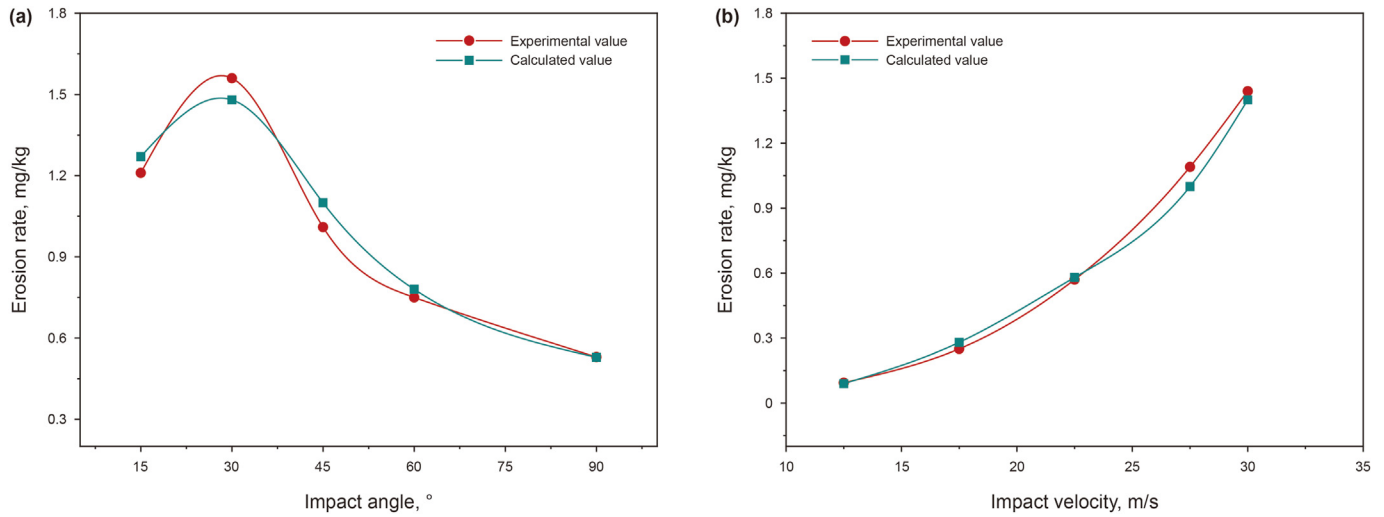


Fig. 7. Comparison of calculated and experimental values (a) Different erosion angles (b) Different impact velocity.

Table 6

The pore size of the ball seat corresponding to each stage.

Stage	Inner diameter, mm	Number	Inner diameter, mm	Number	Inner diameter, mm
2	25.4	9	46.4	16	67.4
3	28.4	10	49.4	17	70.4
4	31.4	11	52.4	18	73.4
5	34.4	12	55.4	19	76.4
6	37.4	13	58.4	20	79.4
7	40.4	14	61.4	21	82.4
8	43.4	15	64.4		

differential pressure sliding sleeves, and the second to 21st stages use sliding sleeves ball seats. Table 6 shows the hole diameter of each stage of the ball seat.

For the numerical simulation, an example of the No. 3 ball seat is taken, and we establish the internal fluid domain of the sliding sleeve ball seat and divide the mesh. The fluid area at the front end of the sliding sleeve ball seat is extended by 150 mm to ensure stable fluid flow into the ball seat. The tapered surface behind the sliding sleeve ball seat will not affect the analysis of the front cone surface, so the tapered surface behind the sliding sleeve ball seat is ignored. For the mesh, hexahedral are used. The number of grids of the sliding sleeve ball seat fluid domain model is about 200,000, and the mesh quality is about 0.8. There is no negative mesh, which meets the calculation requirements of the Fluent software (Fig. 8).

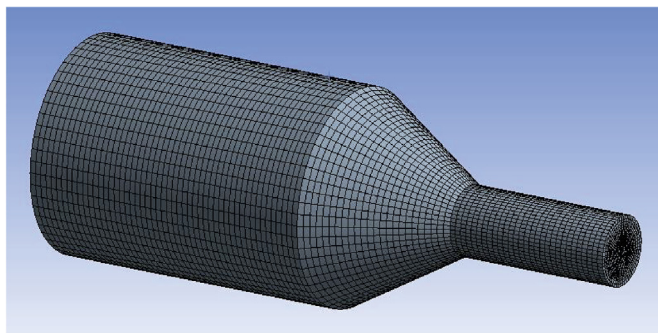


Fig. 8. Mesh model and fluid domain of sliding sleeve ball seat.

4.2. Boundary conditions

The boundary conditions for simulation in this paper are all based on the on-site fracturing conditions. The liquid sand content is 20%–30%, the average sand content is about 25%, and the construction displacement is 2–10 m³/min.

4.2.1. Entrance boundary condition

Water and sand were used in previous experiments, so liquid water was added to the material library. The velocity inlet boundary is adopted and the inlet velocity direction is perpendicular to the inlet end face. The average fluid velocity at the inlet is \bar{u} , turbulence intensity is I , turbulent kinetic energy is k , turbulent dissipation rate is ϵ , and Reynolds number, Re , can be calculated by formulas (13)–(17).

$$\bar{u} = \frac{Q}{S} \tag{13}$$

$$\epsilon = \frac{C_\mu^{0.75} k^{1.5}}{l} \tag{14}$$

$$I = 0.16 \left((Re)^{-1/8} \right) \tag{15}$$

$$k = \frac{3(\bar{u}l)^2}{2} \tag{16}$$

$$Re = \frac{\rho v D_H}{\mu} \tag{17}$$

where Q is the total flow rate, m^3/min ; S is the cross-sectional area, m^2 ; \bar{u} is the average fluid velocity, m/s ; l is the turbulent flow length, m ; C_μ is a constant, taken as 0.09; Re is the Reynolds number; μ is dynamic fluid viscosity, $Pa \cdot s$; ρ is the liquid density, kg/m^3 ; v is the fluid velocity, m/s ; D_H is the hydraulic diameter, m .

According to the field conditions and Eqs. 13–17, the boundary conditions in the simulation process can be calculated, as shown in Table 7.

The particles used in the test are sand grains of the same size, with a density of $2600 kg/m^3$ and a diameter of $0.8 mm$. Due to the relatively high concentration of the particle phase, a dense discrete phase model (DDPM) was applied to simulate the particle-laden flow (Wang et al., 2019).

4.2.2. Export boundary conditions

The flow field at the solid-liquid outlet is treated as fully divergent. Due to the gravity in the pipe string, the fracturing fluid forms a confining pressure at the outlet of the downhole runner model. Thus, the outlet boundary condition of the model is set with the pressure outlet and the particles are assumed to escape completely.

4.2.3. Wall boundary conditions

The erosion rate formulas (11) and (12) of ductile iron and WC determined through experiments in the previous section are set in the generic models of the wall boundary conditions. Among them, the impact angle function of ductile iron is $f(\theta) = -2E - 7\theta^4 + 7.5E - 5\theta^3 - 0.0077\theta^2 + 0.2598\theta$, the impact angle function of WC is $f(\theta) = 3.6E - 6\theta^3 - 0.0005\theta^2 + 0.0288\theta$, the velocity index of ductile iron is $b(v) = 2.2101$ and the velocity index of WC is $b(v) = 2.9694$.

4.2.4. Solver settings

In the staged fracturing of horizontal wells, the fluid has fully developed and stabilized before entering the ball seat, and the flow of fracturing fluid is incompressible, so a velocity-based solver is selected. The discrete method of pressure and the discrete method of momentum are based on the finite volume method (FVM) with second-order upwind styles. The settings of other types of parameters follow the Fluent default algorithm.

4.3. Simulation results and discussion

We analyze the fluid flow velocity inside the sliding sleeve ball seat of different series and obtain the fluid velocity contour plot inside the ball seat of each series number. The flow velocity cloud diagrams of the 4th and 7th stages are presented in Fig. 9. It showed that when the inlet flow rate is the same, the smaller the number of stages, the greater the outlet flow rate. This is because the smaller the number of stages, the smaller the outlet diameter. The sand-

Table 7
Boundary conditions and parameters.

Boundary conditions	Parameter values
Construction displacement, m^3/min	6
Inlet speed, m/s	18.19
Particle ratio, %	30
Turbulence intensity, %	2.8
Hydraulic diameter, m	0.028
Outlet pressure, MPa	50

carrying liquid is restricted by the conical surface of the sliding sleeve ball seat in the process of passing through the ball seat and shrinks toward the axis line. Based on the law of conservation of mass, when the outlet diameter is smaller, the fluid velocity increases.

Due to the different flow fields inside the ball seats of different stages, the erosion and wear analysis of the sliding sleeve ball seats of different stages can get the erosion and wear rate cloud diagram for 20 (stage 2–21) ball seats. In the process of numerical simulation of erosion and wear of sliding sleeve ball seats of all stages, it is found that the wear cloud patterns of the most severe locations of all sliding sleeve ball seats are consistent, but the erosion wear rate is different. Figs. 10 and 11 are the erosion and wear cloud diagrams of stage 4–21 ductile iron material and WC material sliding sleeve ball seat.

It can be seen from Figs. 10 and 11 that the most severe erosion and wear area of the sliding sleeve ball seat of the two materials is the junction of the cone and the small cylindrical surface. This is because the sand particles move with the fracturing fluid in the internal flow channel of the sliding sleeve ball seat and the area close to the wall surface. When the sand particles hit the wall surface, erosive wear occurs. The sand particles are evenly dispersed in the fracturing fluid before flowing into the sliding sleeve ball seat. When the sand-carrying liquid flows into the sliding sleeve ball seat, the trajectory of the sand particles will be restricted by the conical surface of the sliding sleeve ball seat and shrink to the axis line. Due to the effect of inertia, the sand particles in the outer ring of the liquid flow column do not have enough time to mix with the fracturing fluid uniformly, which makes the concentration of sand particles at the cone surface increase. And because the sand-carrying liquid flows from the large diameter area into the small diameter area, the speed of the sand particles also increases, thereby accelerating the erosion and wear effect of the sand particles on the inner wall of the ball seat. It can be seen from the comparison of Figs. 10 and 11 that the wear of ductile iron materials is more uniform, and the local wear of WC materials is more obvious. This is because ductile iron is a plastic material and WC material is a brittle material, so WC is more prone to cracks. However, the erosion rate of WC material under the same conditions is relatively smaller, and its wear resistance is better.

Fig. 12 are the topography of the ball seat (a) before and (b) after erosion (Zheng et al., 2016), and Fig. 12(c) is the erosion rate cloud diagram of the Fluent simulation. The experimental results show that the cone surface of the ball seat is worn and the largest erosion wear area is located at the junction of the cone surface and the small cylinder, which is consistent with the simulation results in this paper.

The erosion rate can be quantified by the erosion depth, which is related to the erosion rate of the ball seat, the density and time of the ball seat.

$$\delta = \frac{3.6 \times 10^6 R_{erosion} t}{\rho} \tag{18}$$

In the formula, δ is the erosion depth, mm ; $R_{erosion}$ is the wear rate, $kg/(m^2 \cdot s)$; ρ is the liquid density, kg/m^3 ; t is the erosion time, s .

Taking WC and ductile iron sliding sleeve ball seat as an example, the morphology change of the sliding sleeve ball seat was analyzed after 10 h of erosion. Taking the intersection of the conical surface of the sliding sleeve ball seat and the small cylindrical surface as the origin, the cross-sections are taken every 1 mm to both sides. There are 15 sections in total. According to the extracted erosion rate of each section, the erosion depth at each section of the sliding sleeve ball seat after 10 h is calculated (Formula (18)). Fig. 13(a) and (b) plot the erosion depth of the cross-section at

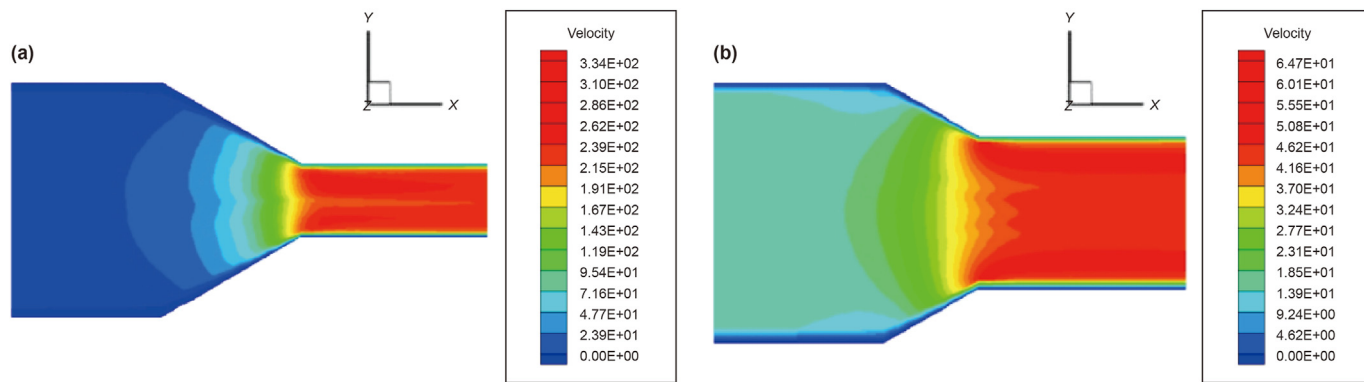


Fig. 9. Fluid velocity cloud diagram inside the ductile iron sliding sleeve ball seat (Unit: m/s) (a) Stage 4 and (b) Stage 13.

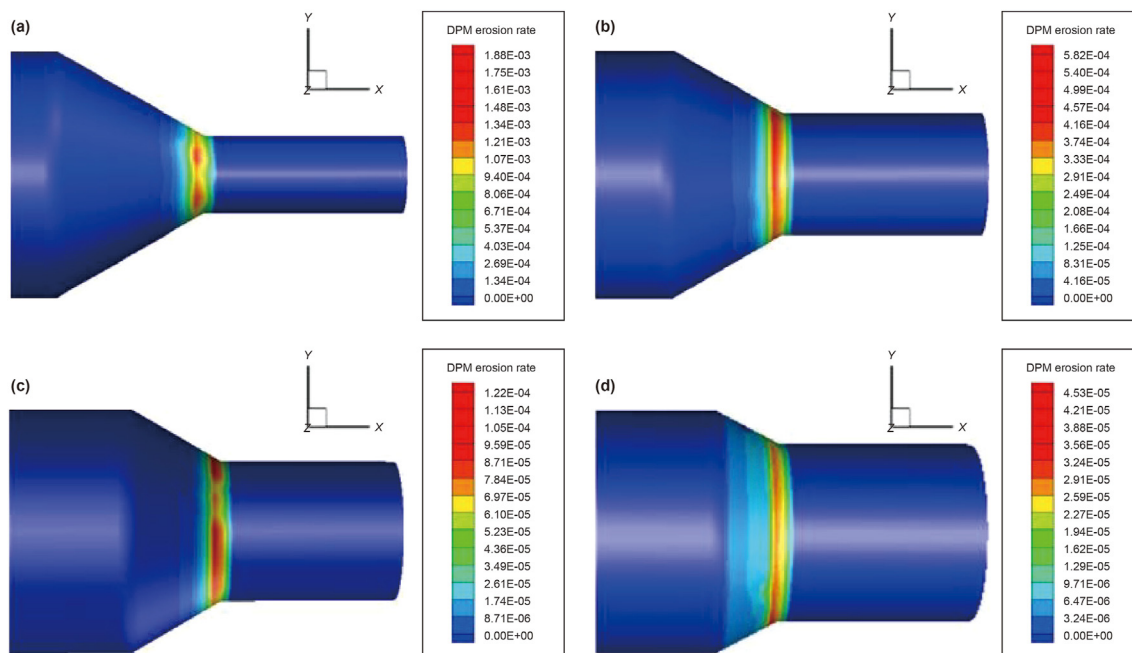


Fig. 10. Erosion wear cloud diagram of ductile iron ball seat (a) stage 4 (b) stage 10 (c) stage 16 (d) stage 21.

different positions of the WC and ductile iron sliding sleeve ball seat, respectively. And taking ductile iron as an example, the topography of the ball seat after 10 h of erosion is drawn, as shown in Fig. 11(b).

Under the same erosion time, the aperture of the sliding sleeve ball seat increases as the number of stages decreases (Fig. 13). The change in the pore diameter of the front side of the junction between the cone and the small cylinder is the largest, gradually decreasing to both sides. If the erosion is carried out for a long time, the final reduced diameter will become a smooth transition zone like a "flare". Each sliding sleeve ball seat of other stages can use this method to predict the morphology of the sliding sleeve ball seat after erosion at any time. This Fluent model can provide not only a basis for predicting the failure time of the ball seat but also guidance for the selection of the sliding sleeve ball seat, the surface treatment method, and the optimal design of the ball seat shape.

5. Conclusion

This paper addresses the sliding sleeve ball seat for both

physical and numerical experiments. A set of erosion models are established by experimental methods to study the erosion and wear laws of different materials by the sand-carrying liquid, and the following conclusions are obtained:

- (1) A prediction model for the erosion rate of ductile iron and WC material ball seats was established. Both calculated values through the model and experimental values obtained were compared and verified. It is found that the error between the two values is no more than 10%. This shows that the calculation model can be effectively used to predict the erosion rate of the ball seat in the actual working condition.
- (2) By comparing the erosion simulation results of ductile iron and WC material, it can be seen that when the erosion angle is 30°, the erosion rate of WC material is lower and its wear resistance is better. The simulation results are similar to the test results.
- (3) The aperture of the sliding sleeve ball seat increases as the working time increases. The change in the pore diameter of the front side of the junction between the cone and the small

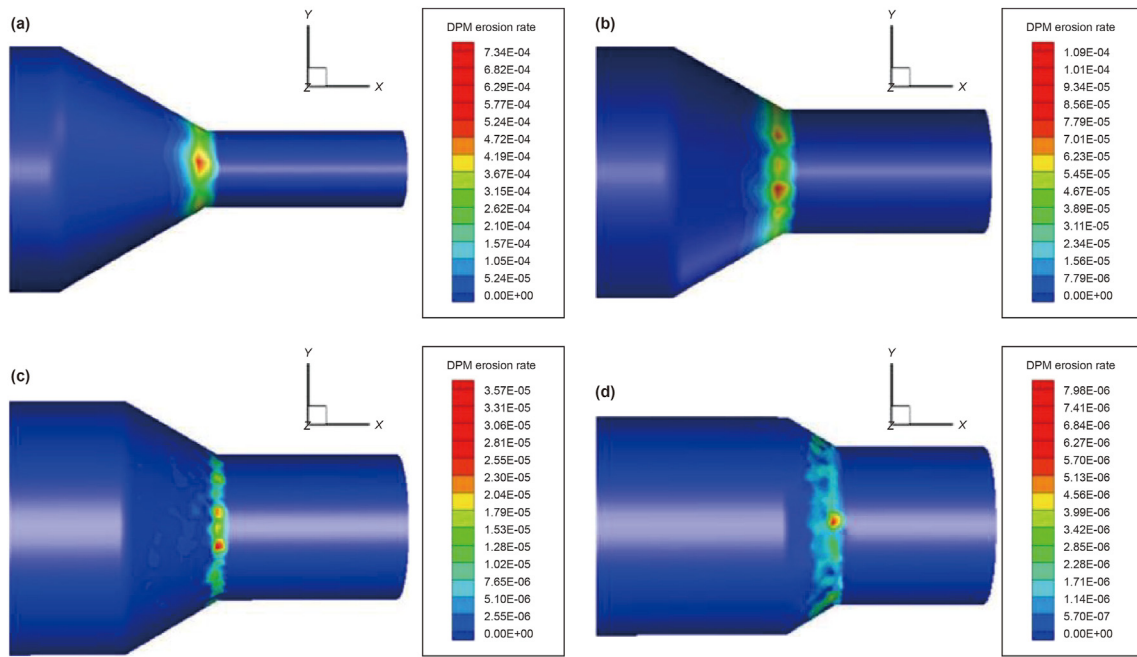


Fig. 11. Erosion wear cloud diagram of WC material ball seat (a) stage 4 (b) stage 10 (c) stage 16 (d) stage 21.

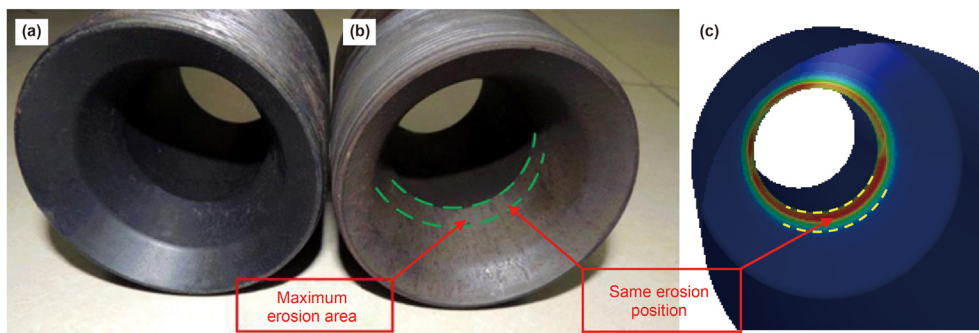


Fig. 12. Morphology of the ball seat (a) before and (b) after erosion © Elsevier 2016 (c) erosion rate cloud diagram of the erosion rate of ball seat.

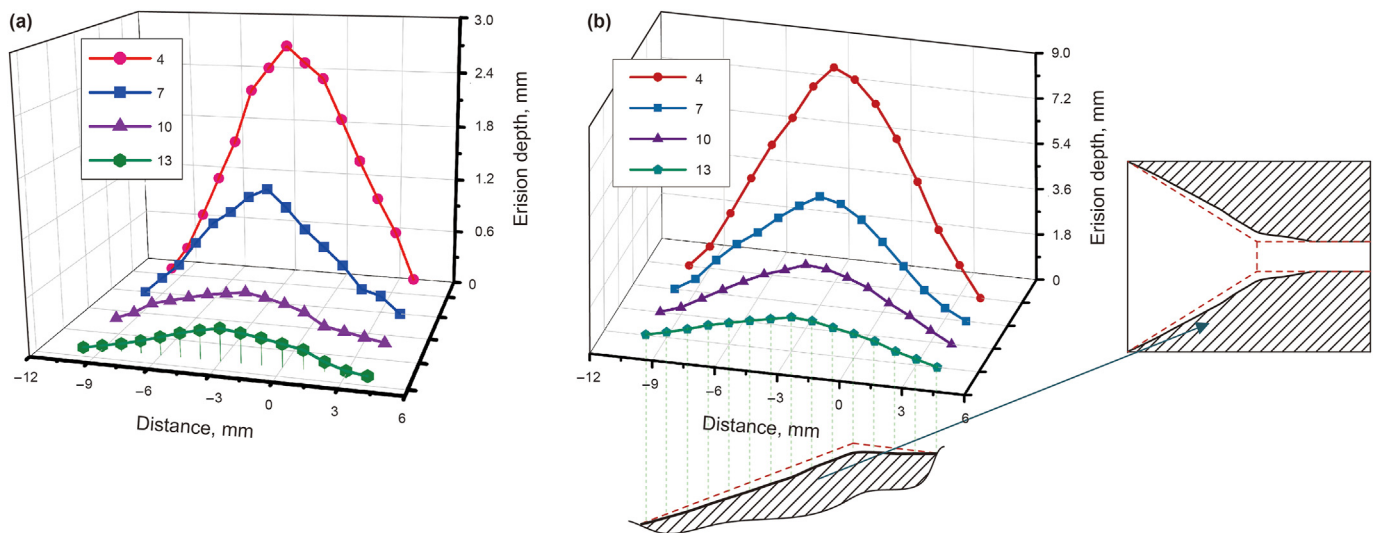


Fig. 13. Erosion depth and morphology of sections of (a) WC and (b) ductile iron ball seats at different positions.

cylinder is the largest, gradually decreasing to both sides. The maximum erosion area of the simulated ball seat is consistent with the experimental results on site. Under the same condition, the lower stage is, the larger the erosion rate is obtained. Therefore, for the multi-stage sliding sleeve ball seat, the method in this study can be used to predict the morphology of each stage sliding sleeve ball seat after erosion at any time, and based on the prediction results, different ball seat materials can be selected. To assure the safety and reliability of the fracturing operation, WC material can be sprayed on the ductile iron material forming a WC coating to enhance the durability of the ball seat material.

Acknowledgments

This research was funded by the National Natural Science Foundation of China (grant number 51675534).

References

- Jung, K.H., Kim, S.J., 2020. Effect of various factors on solid particle erosion behavior of degraded 9Cr-1MoVNb steel with experiment design. *Appl. Surf. Sci.* 506 (144956). <https://doi.org/10.1016/j.apsusc.2019.144956>.
- Liu, Z.G., Wan, S., Nguyen, V.B., Zhang, Y.W., 2014. A numerical study on the effect of particle shape on the erosion of ductile materials. *Wear* 313 (1-2), 135–142. <https://doi.org/10.1016/j.wear.2014.03.005>.
- Miao, W.J., Zhao, L., 2017. Development status and prospect of staged fracturing technology in horizontal wells. *Electron. J. Geotech. Eng.* 2017, 22.
- Nandlal, K., Weijermars, R., 2019. Drained rock volume around hydraulic fractures in porous media: planar fractures versus fractal networks. *Petrol. Sci.* 16 (5), 1064–1085. <https://doi.org/10.1007/s12182-019-0333-7>.
- Nguyen, V.B., Nguyen, Q.B., Liu, Z.G., Wan, S., Lim, C.Y.H., Zhang, Y.W., 2014. A combined numerical–experimental study on the effect of surface evolution on the water–sand multiphase flow characteristics and the material erosion behavior. *Wear* 319 (1-2), 96–109. <https://doi.org/10.1016/j.wear.2014.07.017>.
- Oka, Y.I., Yoshida, T., 2005. Practical estimation of erosion damage caused by solid particle impact: Part 2: mechanical properties of materials directly associated with erosion damage. *Wear* 259 (1-6), 102–109. <https://doi.org/10.1016/j.wear.2005.01.040>.
- Oka, Y.I., Okamura, K., Yoshida, T., 2005. Practical estimation of erosion damage caused by solid particle impact: Part 1: effects of impact parameters on a predictive equation. *Wear* 259 (1-6), 95–101. <https://doi.org/10.1016/j.wear.2005.01.039>.
- Pei, X.H., Wei, S.B., Shi, B., Shen, Z.J., Wang, X.Z., Tong, Z., et al., 2014. Disintegrating fracturing ball used in ball injection sliding sleeve for staged fracturing. *Petrol. Explor. Dev.* 41 (6), 805–809. [https://doi.org/10.1016/S1876-3804\(14\)60097-5](https://doi.org/10.1016/S1876-3804(14)60097-5).
- Safari, M., Rastegari, V., Shahmarvand, S., 2017. Hydraulic fracturing in condensate reservoirs: a simulation study. In: 2017 International Conference on Environmental Impacts of the Oil and Gas Industries: Kurdistan Region of Iraq as a Case Study (EIOGI), vol. 25, pp. 92–96. <https://doi.org/10.1109/EIOGI.2017.8267633>.
- Sepehr, H., Nikrityuk, P., Breakey, D., Sanders, R.S., 2019. Numerical study of crude oil batch mixing in a long channel. *Petrol. Sci.* 16 (1), 187–198. <https://doi.org/10.1007/s12182-018-0276-4>.
- Wang, Z., Zhang, J., Shirazi, S.A., Dou, Y., 2019. Experimental and numerical study of erosion in a non-Newtonian hydraulic fracturing fluid. *Wear* 422, 1–8. <https://doi.org/10.1016/j.wear.2018.12.080>.
- Zhang, Y., Reuterfors, E., McLaury, B.S., Shirazi, S., Rybicki, E., 2006. Comparison of computed and measured particle velocities and erosion in water and air flows. *Wear* 263 (1-6), 330–338. <https://doi.org/10.1016/j.wear.2006.12.048>.
- Zhang, J., Kang, J., Fan, J., Gao, J., 2016. Research on erosion wear of high-pressure pipes during hydraulic fracturing slurry flow. *J. Loss Prev. Process. Ind.* 43, 438–448. <https://doi.org/10.1016/j.jlp.2016.07.008>.
- Zhang, J.X., Bai, Y.Q., Kang, J., Wu, X., 2017. Failure analysis and erosion prediction of tee junction in fracturing operation. *J. Loss Prev. Process. Ind.* 46, 94–107. <https://doi.org/10.1016/j.jlp.2017.01.023>.
- Zheng, C., Liu, Y., Wang, H., Qin, J., Chen, C., Liu, Z., et al., 2016. Finite element analysis and experimental study on the deformation characteristics of an aluminum alloy fracturing ball. *J. Nat. Gas Sci. Eng.* 35, 203–210. <https://doi.org/10.1016/j.jngse.2016.08.037>.
- Zheng, C., Liu, Y., Wang, H., Qin, J., Chen, C., Zhang, S., et al., 2017. Dissolvable fracturing tool based on a controlled electrolytic method. *J. Petrol. Sci. Eng.* 153, 81–87. <https://doi.org/10.1016/j.petrol.2017.03.035>.
- Zhu, H., Qi, Y., 2019. Numerical investigation of flow erosion of sand-laden oil flow in a U-bend. *Process Saf. Environ. Protect.* 131, 16–27. <https://doi.org/10.1016/j.psep.2019.08.033>.